Volume 1 | Number 1 | Jan 2013 | Pages 1–100

Journal of
Materials Chemistry A

Materials for energy and sustainability
www.rsc.org/materialsA

Li⁺

ROYAL SOCIETY
OF CHEMISTRY

ROYAL SOCIETY
OF CHEMISTRY

www.rsc.org/materialsA

Journal Name

ARTICLE

Efficiency enhancement by defect engineering in perovskite photovoltaic cells prepared by evaporated PbI₂/CH₃NH₃I multilayers

Annie Ng,[a] Zhiwei Ren,[a] Qian Shen,[a] Sin Hang Cheung,[b] Huseyin Cem Gokkaya,[a] Gongxun Bai,[c] Jingchuan Wang,[d] Lijun Yang,[d] Shu Kong So,[b] Aleksandra B. Djurišić,[e] Wallace Woon-fong Leung,[d] Jianhua Hao,[c] Wai Kin Chan[f] and Charles Surya[a,*]

We report, for the first time, on the synthesis of perovskite films by thermal annealing of evaporated lead (II) iodide (PbI₂)/methylammonium lead iodide (CH₃NH₃I) multilayers. Detailed characterizations of the resulting films are presented. Our work demonstrates that compact, high quality and uniform perovskite films can be grown using this technique. Optimization of the device structure was achieved by careful design of the layer thickness and the number of PbI₂/CH₃NH₃I pairs used in the formation of the absorber layer. Utilizing additional annealing steps in controlled ambient was shown to result in significant improvement in the device performance. Our experimental data indicate that O₂ treatments may result in substantially reduced trap density in the device and thereby significantly improving the lifetimes of the carriers. A high power conversion efficiency (PCE) of 12.5% was recorded for the champion device.

Introduction

A major scientific breakthrough has been made in the field of photovoltaics with the emergence of organo-metallic perovskite as the absorber material.[1-8] The superior physical properties of this class of materials such as the strong light harvesting capability over a broad region of visible light spectrum,[9] extremely long carrier diffusion lengths,[10,11] broadly tuneable bandgaps,[12] good crystallinity[13,14] and high carrier mobilities[14-16] have satisfied most of the requirements for fabricating high performance solar cells. The rapid development of perovskite-based solar cells has been triggered since the first report on the utilization of organolead halide perovskite as the sensitizer in photovoltaic cells.[17] With the tremendous research efforts contributed from different groups, the power conversion efficiency (PCE) of the perovskite-based solar cells has been boosted dramatically from 3.8%[17] to 19.3%[18] within a short period of time. Significant progress in material engineering,[12,19] modification of device architectures[13,20-26] as well as optimization of fabrication techniques[27-31] have been accomplished leading to substantial enhancements in the device performance. The results clearly indicate huge potential in the development of highly competitive perovskite-based solar cells in the near future.

A number of key factors underlie the fabrication of high efficiency photovoltaic cells (PVCs) such as film coverage and the crystallinity of the absorber layer. Insufficient film coverage results in the reduction in light absorption capability as well as the formation of shunting paths due to the direct contact between the 2,2'7,7'-tetrakis(N,N-di-p-methoxyphenyl-amine)-9,9'-spirobifluorene (spiro-MeOTAD) and titanium(IV) oxide (TiO₂) layers.[32] Effective control of the film morphology is also important to achieve high crystalline films, which is favorable for efficient charge transport.[29,33] There are four reported strategies to prepare perovskite absorber layers for PVCs including one-step precursor deposition,[31] sequential deposition method (or known as two-step method),[27,34] dual-source vapour co-deposition[28] and vapour-assisted solution process.[29] Both one-step precursor deposition and sequential deposition are all-solution-processes with the former involving a single solvent to dissolve the powder mixture of metal halide and organic species, and the latter involving two solvents to dissolve the metal halide and organic species separately. In the one-step deposition technique, the formation of the perovskite layer is achieved by spin-coating or drop-casting the precursor solution on the substrate followed by thermal annealing to complete the formation of perovskite from the precursors. The optimization of the material mixing conditions, concentrations of precursor solutions, type of solvents, annealing temperature

and time are critical for achieving good coverage and high crystalline perovskite films. For typical sequential deposition, PbI_2 in N,N-dimethylformamide (DMF) is first spin-coated on the substrate, which are then dipped into the solution of isopropanol (IPA) containing CH_3NH_3I. The perovskite is formed instantaneously once PbI_2 is exposed to CH_3NH_3I and subsequent thermal annealing of the samples is required to complete the transformation. The sequential deposition method enables better material infiltration into mesoporous TiO_2 and provides better control over the film morphology of perovskite compared to one-step deposition method.[27] Apart from the solution process, perovskite prepared by vapour deposition yielding high efficiency solar cells was reported by M. Liu *et al*.[28] In their work, the lead (II) chloride ($PbCl_2$) and CH_3NH_3I were thermally co-evaporated onto the compact TiO_2-coated FTO glass with varying the composition ratio of $PbCl_2$ to CH_3NH_3I. The vapour-deposited mixed-halide perovskite films exhibit superior uniformity compared to solution-processed films and PCE up to 15.4% was reported using this technique. Recently, Yang and his colleagues have successfully combined the solution and vapour processes to prepare high quality perovskite films,[29] in which PbI_2 was first spin-coated on compact TiO_2-coated FTO glass and subsequently annealed in CH_3NH_3I vapour at 150°C. The resulting perovskite films exhibit large grain size, good surface coverage and high uniformity. Besides, this method avoids the high reaction rate of the precursors in the co-deposition process and prevents film deterioration when an inorganic layer is dipped into an organic solution. A PCE up to 12.1% was reported using this technique with a planar device structure. Among the various deposition techniques, vapour deposition has great potential for large-scale production and is compatible with multijunction fabrication of hybrid tandem solar cells, which are highly desirable for the future development of high-efficiency perovskite-based devices.

In this work, we introduce a modified thermal evaporation method to prepare high quality $CH_3NH_3PbI_3$ absorber layers. For the conventional co-evaporation process, the deposition rates of organic and inorganic species have to be precisely controlled at the same time, which is of great importance in ascertaining the correct compositions of the perovskite film. This situation would become more problematic when preparing mixed-halide perovskites in which a number of precursors may be involved.[35] In contrast with the co-evaporation technique, we demonstrate the formation of high quality perovskite from multilayers of the precursor materials for which film thickness of each layer is the only parameter that needed to be precisely controlled during the deposition process. This technique demonstrates the formation of pinhole-free perovskite films with excellent uniformity. Through the optimization of precursor thickness in each layer and total number of precursor pairs we demonstrate successful fabrication of planar $CH_3NH_3PbI_3$-based PVCs with PCE as high as 12.5%.

In the previous work,[36] we have successfully demonstrated the effect of O_2 post-deposition treatments on the enhancement of photovoltaic performance of solution-processed planar $CH_3NH_3PbI_3$-based solar cells. It was shown that the PCE as well as the reproducibility of the devices, treated with O_2, have been substantially improved compared to the control devices with the entire fabrication processes carried out in an N_2-filled glove box. We have shown that O_2 annealing is essential in enhancing the device efficiency and the reproducibility of perovskite-based PVCs due to its ability in the enhancement of the conductivity of the spiro-MeOTAD layer and the passivation of the traps in the bulk of perovskite layer and the material interfaces. Considering the positive effects of O_2 on the perovskite-based PVCs, we have systematically applied O_2 treatment to each constituent layer of the device separately in order to pinpoint the effects of O_2 annealing on the PCE of the solar cells.

Result and Discussion

Perovskite films were synthesized by thermal annealing of evaporated multilayers of PbI_2 and CH_3NH_3I. Based on the stoichiometry of compound, $CH_3NH_3PbI_3$ is obtained from the reaction of PbI_2 and CH_3NH_3I in a mole ratio of 1:1. The density of PbI_2 and CH_3NH_3I are 6.16 g/cm^3 and 2.235 g/cm^3 respectively.[37] The volume ratio of 1 mole of PbI_2 to 1 mole of CH_3NH_3I is 1:0.95. Thus, the thickness of each constituent layer should be roughly the same while any excess CH_3NH_3I can be removed by spin coating IPA on the top of the evaporated films at the final stage. To optimize the thickness of the constituent precursors a PbI_2/CH_3NH_3I (150 nm/150 nm) bilayer was deposited and annealed in N_2 at 90°C for 1 hour. The corresponding X-ray diffraction (XRD) patterns were measured as illustrated in line (e) of Fig. 1 below.
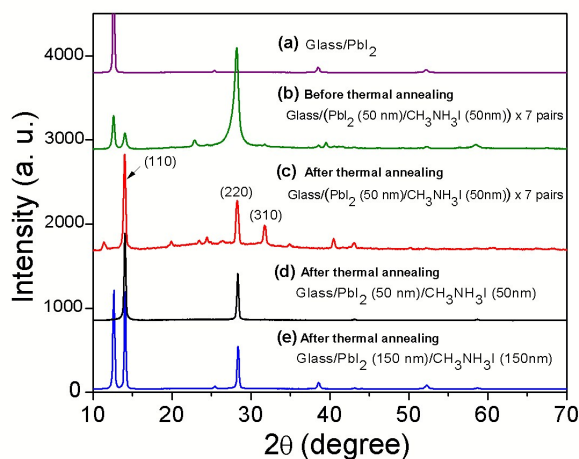
Fig. 1 XRD patterns for different materials deposited on glass.

Comparing the experimental data to line (a) of Fig. 1, which illustrates the XRD pattern for PbI_2, it is clearly noticed that the four diffraction peaks (12.6°, 25.4°, 38.5° and 52.3°) corresponding to the lattice planes of (001), (002), (003) and (004) for PbI_2[27] were also detected in the PbI_2/CH_3NH_3I (150 nm/150 nm) sample even after the sample was thermally

annealed for a period of 2 hours. This indicates that a large portion of unreacted PbI_2 still remains in this bilayer structure. To ensure complete consumption of PbI_2 we reduced the thickness of the individual precursors to 50 nm. Subsequent to thermal annealing a series of diffraction peaks located at 14.0°, 28.4° corresponding to the (110) and (220) planes of $CH_3NH_3PbI_3$ perovskite are found as illustrated in line (d) of Fig. 1. We then fixed the thickness for each precursor layer to 50 nm and deposited a multilayer structure consisting of different number pairs of PbI_2/CH_3NH_3I (50 nm/50 nm). It is noteworthy that the precursor materials PbI_2 and CH_3NH_3I will partially react with each other during the thermal evaporation, particularly at the interfaces between PbI_2 and CH_3NH_3I. The as-prepared films were initially yellowish-brown in color and subsequently changed to reddish-brown after the samples were thermally annealed at 90°C. The color change of the thermally evaporated film before and after thermal annealing is shown in the photographs in Fig. S1 and the corresponding XRD data for the sample consisted of 7 pairs of PbI_2/CH_3NH_3I (50 nm/50 nm) with and without thermal annealing treatment are presented in line (b) and line (c) of Fig. 1 respectively. For the sample without thermal annealing, diffraction peaks contributed from both of PbI_2 and $CH_3NH_3PbI_3$ can be observed. It is noteworthy that the intensity of the diffraction peaks located at 28.4° for the plane of (220) of $CH_3NH_3PbI_3$ at the stage before thermal annealing is more pronounced compared to the other planes. After the sample treated with thermal annealing, diffraction peaks (14.0°, 28.4° and 31.9°) corresponding to $CH_3NH_3PbI_3$ perovskite layer and no obvious diffraction peaks from PbI_2 are detected. At this stage, the main diffraction peak of $CH_3NH_3PbI_3$ is located at 14.0°, which is consistent to many published reports.[27,38,39] The XRD results clearly confirm that utilizing the multilayer deposition technique one can synthesize thick $CH_3NH_3PbI_3$ perovskite films after carefully controlling the thickness of each precursor layer and subsequently treated with thermal annealing. It is noted that the proposed deposition technique is different from the work of Liu et al.[28] and Chen et al.[40] During the multilayer deposition, the substrates are maintained at room temperature instead of elevated temperature.[40] The rapid reaction between precursors, which likely happens during the co-evaporation can be avoided. The limited reaction penetration depth of the precursors can be solved by controlling the thickness of each precursor layer and subsequent thermal annealing step in the glove box.

The morphology of the thermally evaporated films was investigated by scanning electron microscopy (SEM). Figure 2a and 2b illustrate the plan-view images for individual PbI_2 and CH_3NH_3I layers. From Fig. 2a the average grain size for the thermally evaporated PbI_2 layer is found to be < 200 nm whereas the average grain size for the thermally evaporated CH_3NH_3I layer appears to be somewhat larger. Figure 2c illustrates the plan-view image of the as-prepared multilayer film without thermal annealing. At this stage, no perovskite crystalline domains with clear grain boundaries can be observed indicating that the process of perovskite formation is not completed.

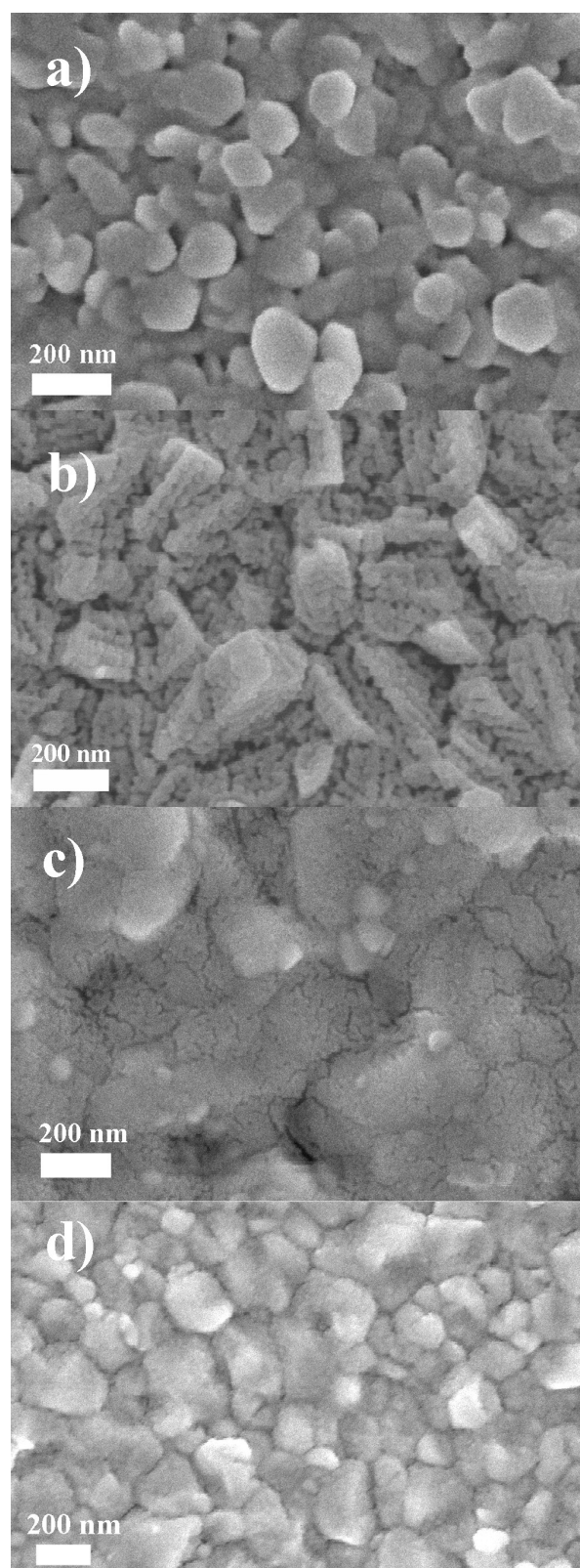
Fig. 2 Top-view SEM images for: (a) as-deposited PbI_2; (b) as-deposited CH_3NH_3I; thermally evaporated PbI_2/CH_3NH_3I sample (c) before and (d) after thermal annealing at 90 °C

However, the film morphology of the multilayer sample illustrated in Fig 2d is changed significantly after the film has

been thermally annealed at 90°C for 1 hour, indicating that an extra step of thermal treatment for the PbI_2/CH_3NH_3I multilayers is necessary to ensure the formation of desired perovskite crystalline domains. The resulting perovskite film exhibits excellent coverage on the TiO_2-coated FTO glass and is essential for the fabrication of high performance photovoltaic devices. The data show that an average grain size of ~300 nm-500 nm can be formed using this technique. It is noteworthy that the variation in the grain size for the perovskite film is found to be relatively smaller for the samples prepared by present method compared to the films prepared by solution process as reported in our previous work.[36] Our results indicate improved uniformity for the films grown by thermal annealing of evaporated PbI_2/CH_3NH_3I multilayers. Atomic force microscopy (AFM) images for the topography and the phase of a typical perovskite film are presented in Fig. 3.

obtained from samples prepared by vapour deposition process.[22,29] It is also observed from the phase image in Fig. 3b that the resulting perovskite film with uniform domain size is formed over an area of 10 μm × 10 μm, which is consistent with our observations from the SEM image.

The absorption of the resulting $CH_3NH_3PbI_3$ perovskite film was confirmed by the UV-vis spectrophotometer. The typical absorption spectrum of $CH_3NH_3PbI_3$, with reported bandgap ~1.5 eV,[41] is obtained and plotted in Fig. 4, which exhibits excellent light harvesting capability up to 800 nm. Furthermore, the formation of the perovskite absorber layer by employing present method can result in films with highly reflective and uniform surface, which ensure high film quality for the spin-coated spiro-MeOTAD HTL on the top of the perovskite.
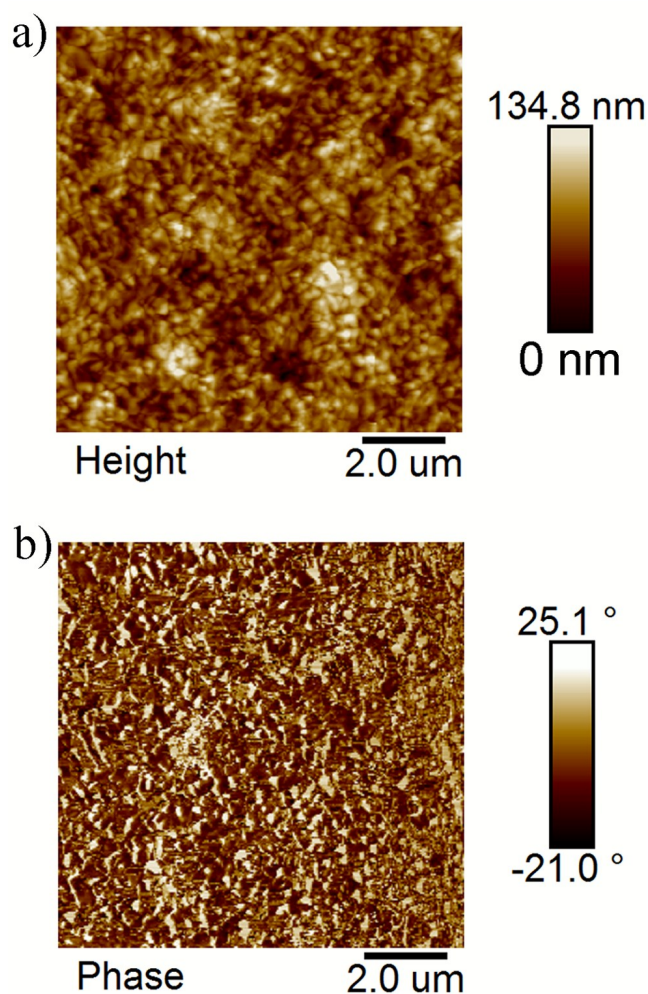

a)

134.8 nm

0 nm

Height   2.0 um

b)

25.1 °

-21.0 °

Phase   2.0 um

Fig. 3 (a) The topography and (b) phase images of a $CH_3NH_3PbI_3$ film prepared by multilayer deposition with thermal annealing at 90°C on TiO_2 coated FTO glass.

Fig. 4 The absorbance spectrum of $CH_3NH_3PbI_3$ prepared by thermal annealing of 2 pair PbI_2/CH_3NH_3I (50 nm/50 nm) at 90°C with the film thickness around 135 nm.

From the figure, the root mean square (rms) roughness of the thermally evaporated perovskite film is determined as 20 nm, which is found to be substantially smaller compared to the solution-processed perovskite films[36] but comparable to results
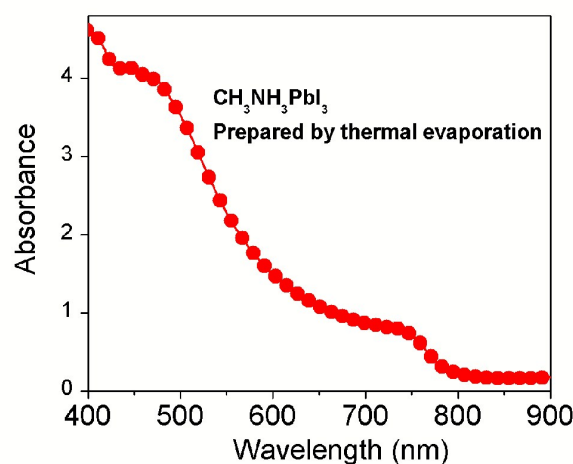
The schematic diagram of the structure of the perovskite-based solar cell is illustrated in Fig. 5a. Figure 5b shows the cross-sectional SEM image for a complete device fabricated using 7 pairs of PbI_2/CH_3NH_3I (50 nm/50 nm) multilayers for the formation of the perovskite absorber. From the SEM image, the total thicknesses of the absorber and spiro-MeOTAD layers are around 470 nm and 175 nm respectively.

Adjusting the thickness of the absorber is a necessary step to optimize the performance of devices. The total thickness of the perovskite layer was varied by controlling the number of precursor pairs. Four different thicknesses of perovskite layers were prepared and the corresponding device parameters are tabulated in Table 1 and the I-V curves of the representative devices are presented in Fig. 6. We found that the open circuit voltage (V_{OC}) is less sensitive to the film thickness compared to other parameters while increasing the film thickness results in a reduction in the fill factors. On the other hand, short circuit current density (J_{SC}) can be substantially improved when the film thickness is increased from 388 nm ± 8 nm to 473 nm ± 9 nm but further increasing the film thickness results in the reduction of J_{SC}. It is not surprising, as the thickness of the

active layer substantially exceeds the reported carrier diffusion lengths ~100 nm for $CH_3NH_3PbI_3$,[10,11] leading to poor carrier collection efficiency. Overall, devices with an absorber layer thickness of 473 nm ± 9 nm (7 pairs) exhibit the highest PCE.
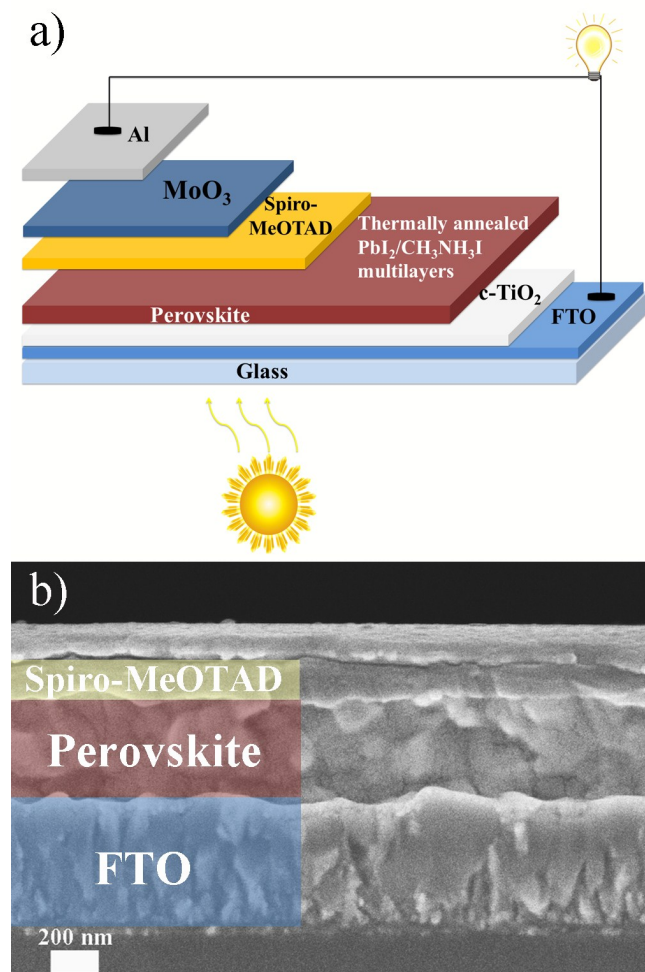

Fig. 5. (a) The schematic diagram of the device configuration of a $CH_3NH_3PbI_3$-based solar cell and (b) the cross-sectional SEM image for the optimal device with 7 pairs of PbI_2/CH_3NH_3I (50 nm/50 nm) multilayers treated with thermal annealing at 90°C.

Table 1 Device parameters for the $CH_3NH_3PbI_3$-based devices with different number of precursor pairs. Average values are determined from 8 devices.

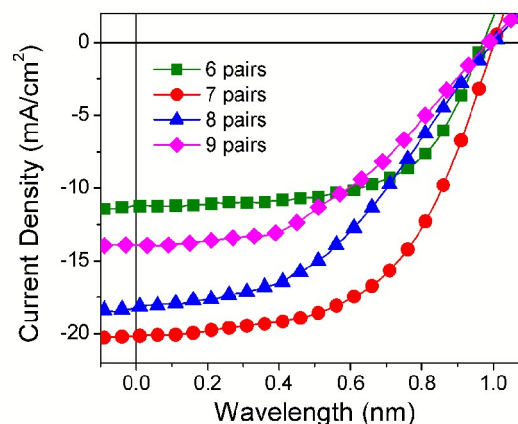| No. of pairs of multilayers (Thickness nm)	V_{oc} (V)	J_{sc} (mA/cm²)	FF	PCE (%)
6 (388± 8)	0.97±0.01	11.7±1.0	0.59±0.02	6.7±0.5
7 (473± 9)	1.00±0.03	20.0±0.8	0.57±0.02	11.4±0.5
8 (542±10)	1.03±0.04	18.0±1.1	0.44±0.04	8.2±0.7
9 (610±7)	1.03±0.06	11.7±5.1	0.43±0.03	5.2±2.5

Fig. 6 The I-V characteristics of the $CH_3NH_3PbI_3$ based devices with different number of pairs of PbI_2/CH_3NH_3I multilayers.

Recent work on perovskite solar cells fabricated using spin-coating technique indicated significant improvements in the device performance after annealing the device in dry O_2 ambient.[36] Detailed experiments were conducted to investigate the impact of O_2 treatment on the thermally evaporated $CH_3NH_3PbI_3$-based solar cells. It is important to note that a practical device consists of different constituent layers and heterojunctions. The impact of the O_2 annealing step may vary throughout the device structure. The work of Abate et al.[42] had pointed out that undercoordinated ions present at the crystal surface may act as trap sites for the charge carriers, leading to the accumulation of charges at material interfaces and causing fast recombination. Passivating these traps sites by external molecules can significantly enhance the device efficiency. Furthermore, it has also been reported that the O_2 exchange process taking place between the atmosphere and semiconductor oxide surface is shown to have significant impact on the operation of the hybrid solar cell.[43,44] To specifically identify the underlying mechanism for the improvement in the PCE due to O_2 annealing we have conducted a detailed investigation, in which the O_2 annealing step was performed at various stages during the device fabrication. Five different types of devices were prepared as indicated in Table 2 in which each constituent layer of the devices was systematically treated in different ambient. The light I-V and EQE characteristics of the representative devices are presented in Fig. 7a and 7b respectively while the corresponding photovoltaic parameters are summarized in Table 2. In general, the trend of the results is consistent with the devices fabricated by spin-coating technique,[36] demonstrating significant improvement in the PCE with O_2 treatment on the perovskite and spiro-MeOTAD layers (type 3, 4 and 5). The EQE results of the devices are also in good agreement with the corresponding I-V performance. For the control devices (type 1), all fabrication processes (except for the sintering of TiO_2 in air) have been carried out in an N_2-filled glove box with O_2 and

H$_2$O less than 0.1 ppm. The *I-V* results of the devices clearly indicate that fabricating the entire device in the inert gas ambient does not yield high PCE, which are different from the case of fabricating organic devices.[45,46]

Table 2 Device parameters for the CH$_3$NH$_3$PbI$_3$-based solar cells with each fabrication stage conducted in different ambient (O$_2$ or N$_2$) and the integrated photocurrent from the EQE spectra are indicated in the bracket. Average values are determined from 8 devices.

| Device Type	Treatment	V_{OC} (V)	J_{SC} (mA/cm^2)	FF	PCE (%)
1	c-TiO$_2$ (Air)/Perovskite(N$_2$)/Spiro-MeOTAD (N$_2$)	0.90 ±0.02	6.9 ±2.0 (5.2)	0.31 ±0.08	1.9 ±0.7
2	c-TiO$_2$ (O$_2$)/Perovskite(N$_2$)/Spiro-MeOTAD (N$_2$)	0.95 ±0.01	9.5 ±2.3(10.8)	0.25 ±0.01	2.3 ±0.6
3	c-TiO$_2$ (Air)/Perovskite(O$_2$)/Spiro-MeOTAD (N$_2$)	1.0 ±0.02	12.0 ±1.2(12.5)	0.31 ±0.01	3.8 ±0.6
4	c-TiO$_2$ (Air)/Perovskite(N$_2$)/Spiro-MeOTAD (O$_2$)	0.98 ±0.01	19.5 ±1.1(18.2)	0.60 ±0.03	11.5 ±0.4
5	c-TiO$_2$ (O$_2$)/Perovskite(O$_2$)/Spiro-MeOTAD (O$_2$)	0.99 ±0.02	21.8 ±1.3(18.3)	0.53 ±0.04	11.4 ±0.9
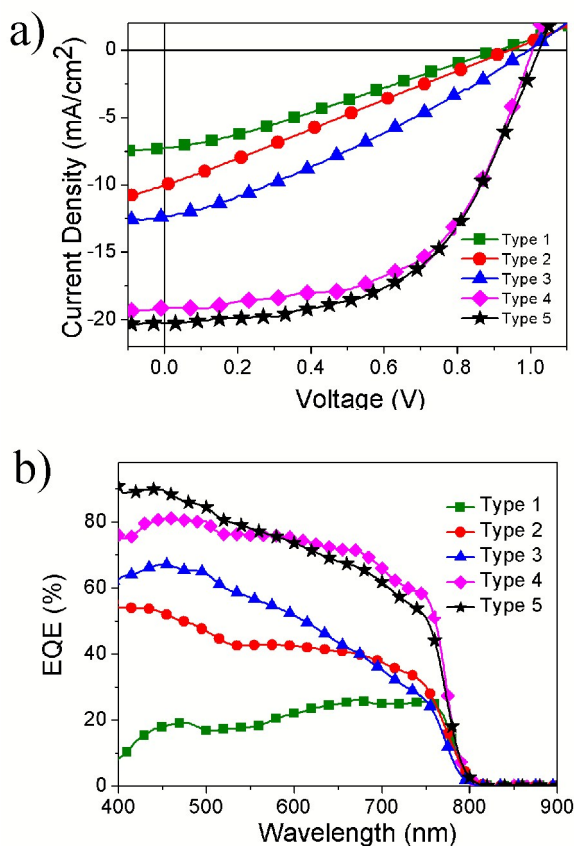
Fig. 7 The *I-V* characteristics of the CH$_3$NH$_3$PbI$_3$ based devices fabricated in different ambient.

For type 2 devices, the TiO$_2$ compact layer was sintered at 450°C with flushing O$_2$ at a flow rate of 4 lit/min while the other processes were conducted in N$_2$ ambient. The overall improvement in PCE for type 3 devices is relatively insignificant. However, the PCE for type 3 devices have been improved significantly from an average of 1.9% to 3.8% when the O$_2$ annealing process was carried out just after the formation of perovskite on TiO$_2$ coated FTO. When comparing the series and shunt resistances determined from the dark *I-V* characteristics of type 3 devices to type 1 and type 2 devices (Fig. S2), their series resistances are similar (~20 Ωcm^2) while the shunt resistance of type 3 devices increases significantly by 1 order of magnitude, indicating that O$_2$ treatment has critical impact on the perovskite layer. The PCEs of type 4 devices were further enhanced by O$_2$ annealing conducted after the deposition of the spiro-MeOTAD layer. The improvement is attributed to the increase in the conductivity of the HTL,[36,47] which is clearly reflected by the reduction in series resistance from ~20 Ωcm^2 to 16 Ωcm^2. It should be noted that O$_2$ annealing in type 4 devices not only impacts on the HTL but also the layers underneath as O$_2$ can diffuse across the layers below the HTL during the annealing process.

The values of the shunt resistance of type 4 devices are similar to type 3 devices, which is attributed to the effect of O$_2$ on the bulk of perovskite and/or material interfaces. The increase in shunt resistance can be an indication of reduced recombination rate within the devices.[48] This can be reflected by the increments of V_{OC} for type 3 and 4 devices, for which the values are consistently enhanced by a maximum of 0.1V, despite the fact that this improvement is less significant compared to the J_{SC}. The averaged J_{SC} of type 4 devices is increased by 12.6 mA/cm^2 and 7.5 mA/cm^2 compared to type 1 and type 3 devices respectively, which is attributed to a combination of factor including the increase in the conductivity of the spiro-MeOTAD layer and the reduction in the recombination rate as suggested by the change in series and shunt resistances. For type 5 devices, we have carried out O$_2$ treatment for every constituent layer. It is interesting to note that the averaged J_{SC} exhibits substantial improvement in type 5 devices compared to all other types of PVCs. However, due to the significant drop in the FF compared to type 2 devices, the overall PCEs for both type 4 and type 5 devices are found to be comparable to each other. It is not clear, based on our existing experimental data alone, the underlying cause for the observed degradation in the FF for type 5 devices despite the fact that the series and shunt resistances of type 5 devices are similar to those of type 4 devices. Further work is needed to identify the physical mechanism responsible for this phenomenon. From Fig. 7b we observe significant improvement in the EQE results from all types of devices compared to the control device, which clearly indicates the positive impact due to O$_2$ treatment. In general, the trend for the EQE is consistent with that of the *I-V* characteristics of the devices as indicated in Fig. 7a. Substantial improvement in the EQE obtained from types 3, 4, and 5 devices demonstrates that the O$_2$ annealing step for the spiro-MeOTAD layer, perovskite layer and also possibly the material

interfaces are essential for the enhancement of the device performance. In contrast to the spin-coated devices,[36] it is noteworthy that raising the annealing temperature during the O_2 treatment above the room temperature does not appear to improve the performance of the devices. Our champion device (type 4) achieves a PCE of 12.5% with a V_{OC} of 0.96 V, J_{SC} of 21.8 mAcm^{-2} and a fill factor of 0.60. We believe that the enhancement in device efficiency from O_2 annealing treatment is not only due to the improved conductivity of spiro-MeOTAD but also due to the reduction in trap density within the perovskite layer and/or material interfaces.[36,42] It is noted that the hysteresis effect is observed in the I-V characteristics for all our devices which generally remained unchanged even at optimized conditions, which suggests that the O_2 annealing treatment is not able to eliminate the origins responsible for the hysteresis effect.[36]

To verify the underlying mechanism of O_2 treatment on perovskite films we have also studied the carrier lifetimes of bare $CH_3NH_3PbI_3$ thermally evaporated on quartz by time-resolved photoluminescence (PL) technique monitored at the emission wavelength as shown in Fig. 8a.
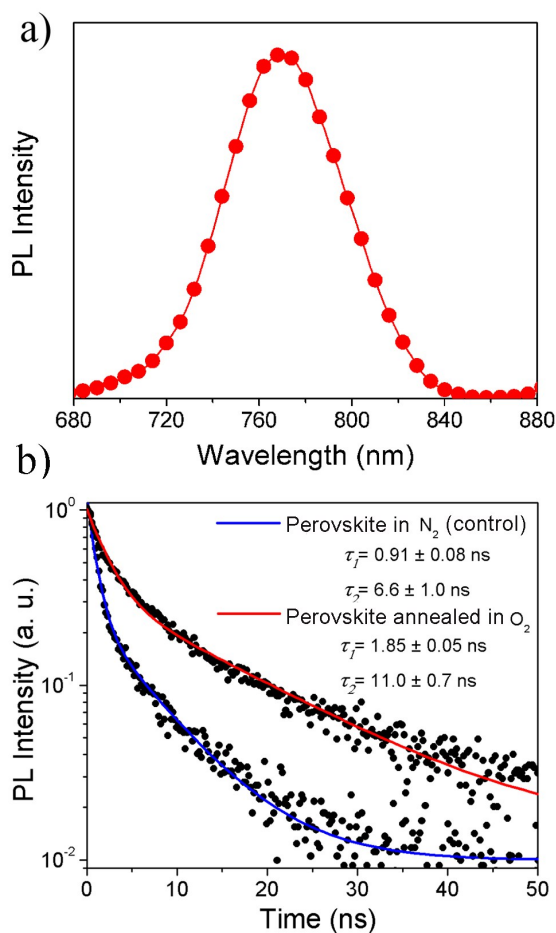
It is noted that the emission peak for the thermally evaporated $CH_3NH_3PbI_3$ film is located at ~770 nm with the calculated optical band gap of ~1.6 eV, which is consistent with reported results of the solution-processed $CH_3NH_3PbI_3$ films.[10,11] The results of the time-resolved PL for the $CH_3NH_3PbI_3$ samples treated in N_2 or O_2 ambient are shown in Fig. 8b. The data are fitted well with the bi-exponential decay function, in which two distinct lifetimes can be determined from the experimental data and the results are in the same order as the reported values in the existing literature.[27,49] For the sample stored in N_2, it is found that τ_1 and τ_2 are 0.91±0.08 ns and 6.6±1.0 ns respectively, indicative of two independent recombination processes in the perovskite material.[49] For the sample annealed in O_2, significant increase in the carrier lifetimes (τ_1=1.85±0.05 ns and τ_2=11.0±0.7 ns) is observed, suggesting that O_2 annealing of the perovskite films can significantly lower the recombination rate, which is most likely due to the reduction in the trap density of the perovskite material.

We have performed photothermal deflection spectroscopy (PDS) to further investigate the impact of O_2 annealing on the defect densities of bare perovskite films on quartz. PDS is an absorption measurement technique with high sensitivity down to the order of 10^{-4}. It can detect the change in the thermal state of the samples due to the nonradiative relaxation of photo-excited carriers. It can be used to characterize the energetic disorder as the exponential decay of the absorption below the bandgap with a characteristic energy named as Urbach energy.[50] This technique had been extensively applied to analyze the electronic defects in amorphous semiconductors and organic semiconductors. The obtained PDS spectra are shown in Fig. 9.

Fig. 8 (a) Steady-state of PL spectrum of the $CH_3NH_3PbI_3$ film on quartz (b) the time-resolved PL of the bare thermally annealed perovskite film on quartz with or without O_2 post-deposition treatment.
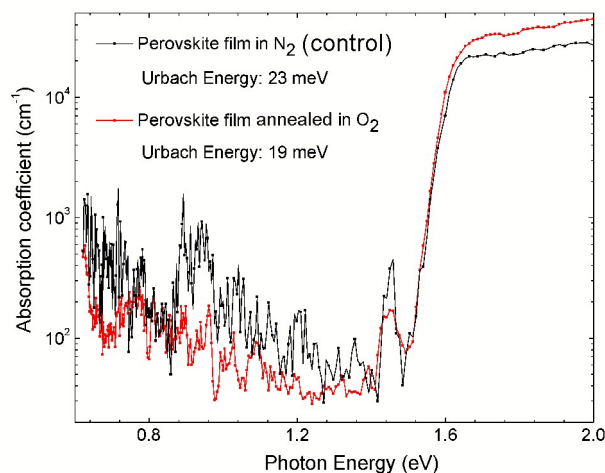

Fig. 9 PDS spectra of the thermally annealed $CH_3NH_3PbI_3$ on quartz with and without O_2 treatment.

It is found that the Urbach energy is substantially reduced from 23 meV for the control sample to 19 meV for the O_2 annealed sample, indicating that the perovskite layer annealed in O_2 exhibits a much sharper bandedge.[51] Meanwhile, it is

observed that the sub-bandgap absorption for the sample without O_2 annealing is more significant compared to the O_2 annealed sample, suggesting that O_2 treatment had led to substantial passivation of sub-bandgap states within the perovskite layer, which is in good agreement with our previous presumption. This is also consistent with the observed improvements in the PCE and the EQE of the devices, for which the perovskite films have been treated with O_2 (type 3, 4 and 5). However, based on the experimental results so far, it cannot identify specifically whether the O_2 annealing also has impacts on the interfaces of each constituent layer of the devices. More experiments are needed to be conducted in order to verify this issue.

Conclusion

High quality $CH_3NH_3PbI_3$ perovskite films have been successfully demonstrated by the thermal annealing of PbI_2/CH_3NH_3I (50 nm/50 nm) multilayers. The technique provides a more precise control over the absorber layer thickness as well as its composition in a straightforward manner. The process ensures high reproducibility of the devices and is compatible with large-scale production processes. The treatment for each constituent layer of the device structure in O_2 and its impact on the performance of the solar cell are investigated systematically. The results suggest that O_2 treatment is crucial for yielding high performance $CH_3NH_3PbI_3$-based solar cells. Under the optimized conditions, the champion device exhibits PCE as high as 12.5% by adopting the proposed deposition technique and O_2 treatment.

Experimental

Patterned FTO coated glass substrates with a sheet resistance of 7-10 $\Omega/\square$ were purchased from KINTEC company. Lead (II) iodide (purity 99.999%, PbI_2), titanium (IV) isopropoxide (TTIP), lithium bis(trifluoromethylsulphonyl)-imide (Li-TFSI), 4-tert-butylpyridine (tBP), N,N-dimethyl-formamide (DMF) and MoO_3 were purchased from Sigma-Aldrich while spiro-MeOTAD (purity> 99.5%) was purchased from Luminescence Technology Corp. Methylammonium iodide (CH_3NH_3I) was supplied by Dyenamo. All chemicals were used as received.

The patterned FTO on glass substrates were cleaned sequentially by ultrasonication in toluene, acetone, ethanol and deionized water. The substrates were then blown dry by nitrogen gas which was then exposed to UV-ozone for 20 min prior to the deposition of the compact TiO_2 layer. For the formation of the TiO_2 film, a mildly acidic diluted TTIP solution (1.25 ml) in ethanol (25 ml) was spin coated on the FTO substrates at 3000 rpm followed by sintering at 450°C for 2 hours in air or with an O_2 flow at 4 lit/min. The formation of the absorber layer of the device was achieved by thermal evaporation of multilayers of PbI_2/CH_3NH_3I directly on the compact TiO_2 layer followed by a thermal annealing step in N_2 ambient at 90°C for 1 hour. The prepared samples with

perovskite layer were stored in N_2 filled glove box or O_2 (high purity grade >99.9%) ambient at a flow rate of 2 lit/min for 12 hours. Systematic optimization of the device structure was performed in which complete devices with different periods of PbI_2/CH_3NH_3I multilayers were deposited. The HTL solution was prepared by dissolving spiro-MeOTAD (80 mg/ml) in chlorobenzene with the additives of Li-TFSI (17.5 μL from a stock solution of 520 mg/ml in acetonitrile) and 29μL of tBP. The solution was then spin-coated on the top of the perovskite layer at 4500 rpm. The prepared samples with spiro-MeOTAD on top were stored in N_2 or O_2 (2 lit/min) ambient for 12 hours. Finally, electrodes (MoO_3/Al (15 nm/120 nm)) were deposited by thermal evaporation through a shadow mask and the device area was 0.09 cm². MoO_3/Al electrodes are used in our devices due to its cost-effectiveness compare to commonly used electrodes such as Au and Ag, which is an important factor for future large-scale production. The devices were encapsulated in N_2 filled glove box before the *I-V* measurement.

The *I-V* characteristics of the devices were measured by using a B1500A semiconductor parameter analyzer under the calibrated ABET Technologies SUN 2000 solar simulator equipped with an AM 1.5 filter at 100 mW/cm². The *I-V* curves were obtained from the reverse scan from 1.2 V to -0.2 V at a scan rate of 0.33 V/s. External quantum efficiency (EQE) was measured by a QE system from Enli Technology Co. Ltd. The surface morphologies of the films were characterized by atomic force microscopy (AFM) in the tapping mode using a Bruker NanoScope 8. UV-visible spectroscopy was performed by using a UV-2550 Shimadzu UV-VIS spectrophotometer for the perovskite film thermally evaporated on quartz. X-ray diffraction (XRD) peaks of the samples were obtained by using a Rigaku SmartLab X-ray diffractometer with Cu Kα radiation in a step of 0.01° and θ-2θ scan mode from 10° to 70°. Scanning electron microscopy (SEM) was performed by using JEOL JSM-6335F field emission scanning electron microscope. Time-resolved photoluminescence signals of perovskite film with or with O_2 treatment were recorded by using an Edinburgh FLSP920 spectrophotometer installed with the excitation source of 485 nm picosecond pulsed diode laser in the average power of 0.15 mW. For PDS measurement, the perovskite film was deposited on quartz substrate and immersed in FC-72, a monochromatic light beam, which was chopped at 13 Hz, was shined to the sample and a laser was at the perpendicular side so that it was deflected periodically, a position sensor, connected with a lock in amplifier, was placed on the other side so that the deflection signal was measured.

Notes and references

[a] Department of Electronic and Information Engineering, The Hong Kong Polytechnic University, Hong Kong SAR
[b] Department of Physics, Hong Kong Baptist University, Hong Kong SAR
[c] Department of Applied Physics, The Hong Kong Polytechnic University, Hong Kong SAR

d Department of Mechanical Engineering, The Hong Kong Polytechnic University, Hong Kong SAR
e Department of Physics, The University of Hong Kong, Pokfulam, Hong Kong SAR
f Department of Chemistry, The University of Hong Kong, Pokfulam, Hong Kong SAR

Correspondence and requests for materials should be addressed to Prof. C. Surya (charles.surya@polyu.edu.hk)

1   H. –S. Kim, S. H. Im, and N. –G. Park, *J. Phys. Chem. C*, 2014, **118**, 5615-5625.

2   S. Kazim, M. K. Nazeeruddin, M. Grätzel and S. Ahmad, *Angew. Chem. Int. Ed.*, 2014, **53**, 2812-2824.

3   P. Gao, M. Grätzel and M. K. Nazeeruddin, *Energy Environ. Sci.*, 2014, **7**, 2448-2463.

4   T. C. Sum and N. Mathews, *Energy Environ. Sci.*, 2014, **7**, 2518-2534.

5   M. A. Green, A. Ho-Baillie and H. J. Snaith, *Nat. Photonics*, 2014, **8**, 506-514.

6   S. Gamliel and L. Etgar, *RSC Adv.*, 2014, **4**, 29012-29021.

7   P. P. Boix, K. Nonomura, N. Mathews and S. G. Mhaisalkar, *Mater. Today*, 2014, **17**, 16-23.

8   H. J. Snaith, *J. Phys. Chem. Lett.*, 2013, **4**, 3623-3630.

9   J. –H. Im, C. –R. Lee, J. –W. Lee, S. –W. Park and N. –G. Park, *Nanoscale*, 2011, **3**, 4088-4093.

10 S. D. Strank, G. E. Eperon, G. Grancini, C. Menelaou, M. J. P. Alcocer, T. Leijtens, L. M. Herz, A. Petrozza and H. J. Snaith, *Science*, 2013, **342**, 341-344.

11 G. Xing, N. Mathews, S. Sun, S. S. Lim, Y. M. Lam, M. Grätzel, S. Mhaisalkar, T. C. Sum, *Science*, **342**, 344-347.

12 G. E. Eperon, S. D. Strank, C. Menelaou, M. B. Johnston, L. M. Herz and H. J. Snaith, *Energy Environ. Sci.*, 2014, **7**, 982-988.

13 M. M. Lee, J. Teuscher, T. Miyasaka, T. N. Murakami and H. J. Snaith, *Science*, **338**, 2012, 643-647.

14 C. C. Stoumpos, C. D. Malliakas and M. G. Kanatzidis, *Inorg. Chem,* 2013, **52**, 9019-9038.

15 G. Hodes, *Science*, 2013, **342**, 317-318.

16 D. B. Mitzi, *Prog. Inorg. Chem.*, 2007, **48**, 1-201.

17 A. Kojima, K. Teshima, Y. Shirai and T. Miyasaka, *J. Am. Chem. Soc.*, 2009, 131, 6050-6051.

18 H. Zhou, Q. Chen, G. Li, S. Luo, T. Song, H. –S. Duan, Z. Hong, J. You, Y. Liu, Y. Yang, *Science*, 2014, **345**, 542-546.

19 F. Hao, C. C. Stoumpos, D. H. Cao, R. P. H. Chang and M. G. Kanatzidis, *Nat. Photonics*, 2014, **8**, 489-494.

20 L. Etgar, P. Gao, Z. Xue, Q. Peng, A. K. Chandiran, B. Liu, M. K. Nazeeruddin and M. Grätzel, *J. Am. Chem. Soc.*, 2012, **134**, 17396-17399.

21 J. M. Ball, M. M. Lee, A. Hey and H. J. Snaith, *Energy Environ. Sci.*, 2013, **6**, 1739-1743.

22 O. Malinkiewicz, A. Yella, Y. H. Lee, G. M. Espallargas, M. Grätzel, M. K. Nazeeruddin and H. J. Bolink, *Nat. Photonics*, 2014, **8**, 128-132.

23 A. Abrusci, S. D. Stranks, P. Docapmo, H. –L. Yip, A. K. –Y. Jen, H. J. Snaith, *Nano Lett.*, 2013, **13**, 3124-3128.

24 S. Dharani, H. K. Mulmudi, N. Yantara, P. T. T. Trang, N. G. Park, M. Graetzel, S. Mhaisalkar, N. Mathews and P. P. Boix, *Nanoscale*, 2014, **6**, 1675-1679.

25 D. –Y. Son, J. –H. Im, H. –S. Kim and N. –G. Park, *J. Phys. Chem. C*, 2014, **118**, 16567-16573.

26 D. Bi, G. Boschloo, S. Schwarzmüller, L. Yang, E. M. J. Johansson, and A. Hagfeldt, *Nanoscale*, 2013, **5**, 11686-11691.

27 J. Burschka, N. Pellet, S. –J. Moon, R. Humphry–Baker, P. Gao, M. K. Nazeeruddin and M. Grätzel, *Nature*, 2013, **499**, 316-319.

28 M. Liu, M. B. Johnston and H. J. Snaith, *Nature*, 2013, **501**, 395-398.

29 Q. Chen, H. Zhou, Z. Hong, S. Luo, H. –S. Duan, H. –H. Wang, Y. Liu, G. Li and Y. Yang, *J. Am. Chem. Soc.*, 2014, **136**, 622-625.

30 M. J. Carnie, C. Charbonneau, M. L. Davies, J. Troughton, T. M. Watson, K. Wojciechowski, H. Snaith and D. A. Worsley, *Chem Commun.*, 2013, **49**, 7893-7895.

31 M. Xiao, F. Huang, W. Huang, Y. Dkhissi, Y. Zhu, J. Etheride, A. Gray–Weale, U. Bach, Y. –B. Cheng and L. Spiccia, *Angew. Chem. Int. Ed.*, 2014, **53**, 1-7.

32 G. E. Eperon, V. M. Burlakov, P. Docampo, A. Goriely and H. J. Snaith, *Adv. Funct. Mater.*, 2014, **24**, 151-157.

33 M. Saliba, K. W. Tan, H. Sai, D. T. Moore, T. Scott, W. Zhang, L. A. Estroff, U. Wiesner and H. J. Snaith, *J. Phys. Chem. C*, 2014, **118**, 17171-17177.

34 Y. Wu, A. Islam, X. Yang, C. Qin, J. Liu, K. Zhang, W. Peng and L. Han, *Energy Environ. Sci.*, 2014, **7**, 2934-2938.

35 N. J. Jeon, J. H. Noh, Y. C. Kim, W. S. Yang, S. Ryu and S. I. Seok, *Nat. Mater.*, 2014, **13**, 897-903.

36 Z. Ren, A. Ng, Q. Shen, H. C. Gokkaya, J. Wang, L. Yang, W. –K. Yiu, G. Bai, A. B. Djurišić, W. W. –F. Leung, J. Hao, W. K. Chan and C. Surya, *Sci. Rep.* 2014, **4**, 6752 1-6.

37 L.Wagner, *Zeitschrift für Kristallographie - Crystalline Materials*, 1907, **43**, 148-201.

38 J. –Y. Jeng, Y. –F. Chiang, M. –H. Lee, S. –R. Peng, T. –F. Guo, P. Chen and T. –C. Wen, *Adv. Mater.,* 2013, **25**, 3727-3732.

39 J. Qiu, Y. Qiu, K. Yan, M. Zhong, C. Mu, H. Yan and S. Yang, *Nanoscale*, 2013, **5**, 3245-3248.

40 C. –W. Chen, H. –W. Kang, S. –Y. Hsiao, P. –F. Yang, K. –M. Chiang and H. –W. Lin, *Adv. Mater.*, 2014, **26**, 6647-6652.

41 H. S. Kim, C. R. Lee, J. H. Im, K. B. Lee, T. Moehl, A. Marchioro, S. J. Moon, R. Humphry-Baker, J. H. Yum, J. E. Moser, M. Grätzel and N. G. Park, *Sci. Rep.*, 2012, **2**, 591 1-7.

42 A. Abate, M. Saliba, D. J. Hollman, S. D. Stranks, K. Wojciechowski, R. Avolio, G. Grancini, A. Petrozza and H. Snaith, *Nano Lett.*, 2014, **14**, 3247-3254.

43 M. Lira-Cantu, K. Norrman, J. W. Andreasen, N. Casan-Pastor and F. C. Krebs, *J. Electrochem. Soc.*, 2007, **154**, B508-B513.

44 M. Lira-Cantu and F. C. Krebs., *Sol. Energy Mater & Sol. Cells,* 2006, **90**, 2076-2086.

45 F. So and D. Kondakov, *Adv. Mater.*, 2010, **22**, 3762-3777.

46 M. Hermenau, M. Riede, K. Leo, S. A. Gevorgyan, F. C. Krebs and K. Norrman, *Sol. Energy Mater & Sol. Cells*, 2011, **95**, 1268-1277.

47 U. B. Cappel, T. Daeneke, U. Bath, *Nano Lett.*, 2012, **12**, 4925-4931.

48 O. Breitenstein, J. P. Rakotoniaina, M. H. Al Rifai and M. Werner, *Prog. Photovolt: Res. Appl.*, 2004, **12**, 529-538.

49 Q. Chen, H. Zhou, T. –B Song, S. Luo, Z. Hong, H. –S. Duan, L. Dou, Y. Liu and Y. Yang, *Nano Lett.* 2014, **14**, 4158-4163.

50 S. D. Wolf, J. Holovsky, S. –J. Moon, P. Löper, B. Niesen, M. Ledinsky, F. –J. Haug, J. –H. Yum and C. ballif, *J. Phys. Chem. Lett.*, 2014, **5**, 1035-1039.

TOC
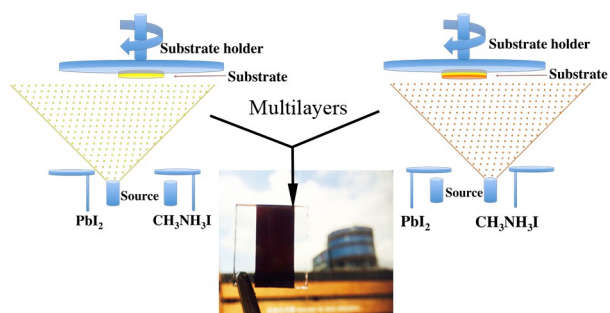
Development of 12.5% $CH_3NH_3PbI_3$-based solar cells from the annealing of thermally evaporated PbI_2/CH_3NH_3I multilayers. Significant enhancement of device performance is achieved through trap engineering in well controlled ambient.